prosthesis

MDPI

Article

Improvement in Mechanical Properties and Anti-Adhesion Activity in Maxillofacial Silicones with Pumpkin Extract Nanoparticles

Taqwa Majid AbdulHussein * and Thekra Ismael Hamad

Department of Prosthodontics, College of Dentistry, University of Baghdad, Baghdad 10071, Iraq; thikra.ismail@codental.uobaghdad.edu.iq

* Correspondence: taqwamajid20@gmail.com

Abstract

Background/Objectives: The deterioration of maxillofacial silicone elastomers is caused by microbial colonization and mechanical failure. Traditional inorganic nanofillers influence the elasticity of materials and their surface hygiene. This study provides a two-phase evaluation of mechanically milled pumpkin (*Cucurbita pepo*) extract nanoparticles (PE-NPs) to evaluate the in vitro anti-adhesion efficacy, mechanical properties, and surface characteristics of VST-50 maxillofacial silicone. **Methods:** In Phase I (Screening Phase), a comparison was made between conventional direct mixing and a newly developed multi-step catalyst-mediated mixing method. The preliminary assessment of anti-adhesion activity against *Staphylococcus epidermidis* (*S. epidermidis*), Shore A hardness, and tear strength was carried out at concentrations of 0, 0.5, 1.0, 1.5, and 2.0 wt.%. In Phase II (Characterization Phase), using the optimized fabrication protocol, final assessment of ultimate tensile strength (UTS), percentage elongation, profilometer surface roughness (Ra), and optical contact angle (Wettability) was carried out. Microstructural characterization was executed using FTIR, FE-SEM/EDX, XRD, and 3D Atomic Force Microscopy (AFM). **Results:** Phase I displays that the catalyst-mediated mixing effectively facilitated processing within the siloxane matrix, resulting in homogeneous nanoparticle dispersion. PE-NPs exhibited a concentration-dependent anti-adhesion response, achieving 95.7% anti-adhesion activity at 2.0 wt.% while improving tear strength and balancing hardness. Phase II demonstrated that 1.5 wt.% represented the concentration providing the most favorable overall balance, significantly enhancing tensile strength (10 [10–10.25] MPa) and elongation percentage (592.26 ± 47.97%). Macro-roughness and contact angles remained statistically unchanged ($p > 0.05$), maintaining baseline surface wettability. However, AFM nanomorphology revealed that 1.5 wt.% PE-NPs effectively filled matrix micro-voids, decreasing nanoscale roughness to 18.88 nm. Agglomeration was captured at 2.0 wt.%, resulting in suboptimal mechanical performance. **Conclusions:** Incorporating 1.5 wt.% organic PE-NPs via a multi-step catalyst integration technique provides an eco-friendly, strong strategy among the evaluated concentrations to enhance initial in vitro mechanical and anti-adhesion properties among the evaluated concentrations without altering baseline surface roughness.

Keywords: maxillofacial silicone; pumpkin extract nanoparticles; *Staphylococcus epidermidis*; biomaterial reinforcement; interfacial adhesion; surface topology

Check for updates

Academic Editor: Andrea Scribante

Received: 14 July 2026
Revised: 22 September 2026
Accepted: 23 September 2026
Published: 26 September 2026

Copyright: © 2026 by the authors. Licensee MDPI, Basel, Switzerland. This article is an open access article distributed under the terms and conditions of the Creative Commons Attribution (CC BY) license.

1. Introduction

Since the 1960s, silicone elastomers, especially polydimethylsiloxane, have become the preferred materials because they are chemically inert, biocompatible, color-stable, and easy to work with. They may be colored on the inside and outside to look authentic and to keep bacteria from growing with minimal effort [1].

Despite these favourable traits, ultraviolet light, humidity, extreme temperatures, biological fluids, disinfectants, pollutants, mechanical stress, and chemical reactions all damage maxillofacial prostheses. These lead to hardening, increased stiffness, decreased flexibility, color changes, and the leaching of low-molecular-weight compounds that affect both the prosthesis and the patient [2]. Microbial colonization and biofilm formation on silicone surfaces may result in material deterioration, discoloration, and soft-tissue inflammation, thereby reducing prosthesis lifetime [3] *S. epidermidis* is a prominent opportunistic pathogen among the related bacteria due to its ability to form biofilms on biomaterial surfaces [4].

To treat these combined biological and mechanical deficiencies, modern dental biomaterial research has shifted toward nanofiller reinforcement. While inorganic additions such as nano-$BaTiO_3$, nano-Al_2O_3, or carbon nanofibers have demonstrated considerable success in enhancing mechanical thresholds, they often generate problems including increased material rigidity, toxic surfactant dependencies, altered cosmetic translucency, or increased surface roughness that promote further biofilm formation [5–7].

Research on natural and organic additives has acquired more attention than inorganic fillers. Investigations into pomegranate peel and date seeds revealed that natural powders can significantly enhance the modulus of elasticity, provided a homogeneous structure is gotten [8].

Investigations into herbal fillers such as thyme and sage (at 5–15 wt.%) showed that grain morphology and size are essential in influencing rebound resilience. These investigations focused on the fact that although the chemical backbone remains stable, natural fillers may affect surface wettability (contact angle) and roughness, which are essential for the prosthesis's physical interaction with the surrounding environment [9].

Pumpkin (*Cucurbita pepo*) extract contains phenolic and flavonoid compounds that have antibacterial activity against oral pathogens [8]. Nanoscale particle reduction may further enhance the bioavailability and surface activity of these phytochemicals [9].

Pumpkin extract comprises a complex array of fatty acids and fiber components that may function as natural "bridging" agents within the silicone elastomer [10,11].

No research has evaluated the synergistic incorporation of Pumpkin Extract Nanoparticles into maxillofacial elastomers; given the complex nature of polymer reinforcement, a linear evaluation can fail to identify processing flaws. Therefore, this study adopts a structured two-phase design. In Phase I (screening phase), nanoparticles are produced; mixing is improved to overcome hydrodynamic barriers through microstructural confirmation and testing of tear resistance, hardness, and anti-adhesion activity; then Phase II (characterizing phase) includes advanced details of tensile strength, macroscopic and nanoscopic surface topographies, and wettability profiles. The hypothesis was that enhanced loading of Pumpkin Extract Nanoparticles would significantly enhance the biological resistance and mechanical properties of RTV silicone while evaluating their surface anti-adhesion performance.

2. Materials and Methods

2.1. Summary of Study Design

The testing process, as shown in Figure 1, was divided into two stages to complete evaluation and prevent structural defects that originate from filler aggregation:

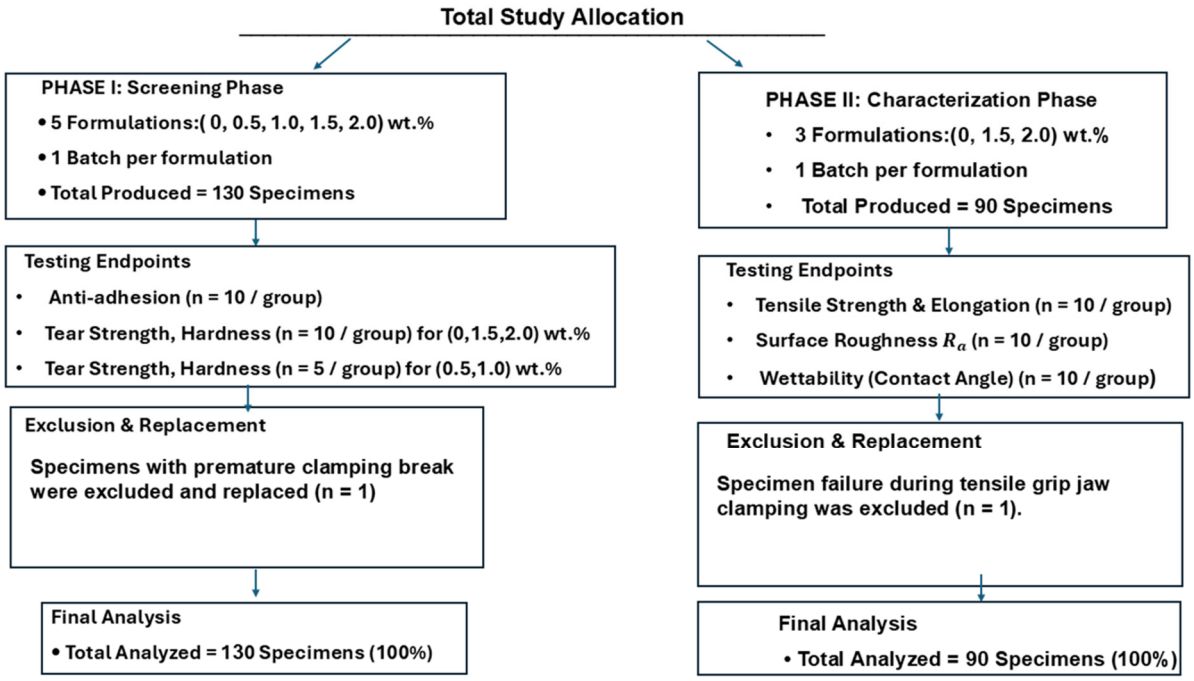


Figure 1. Flow Chart for the Allocation of Experimental Samples. Representative flow diagram showing sample allocation, formulation of dedicated batches prepared separately for Phase I and Phase II for each concentration level, allocation of end-point testing experiments (n = 10 for anti-adhesion and Phase II; n = 5 or 10 for Phase I mechanical tests), rules for specimen rejection, and number of specimens allocated to Phase I (screening) and Phase II (characterization).

Phase I (Screening Phase): Designed to improve the processing basis, confirming chemical compatibility of crystalline phases via FTIR and XRD analyses, and determining preliminary measuring properties across a concentration range (0, 0.5,1.0, 1.5, and 2.0 wt.%).

Phase II (Characterization Phase): Focused on doing advanced physical, mechanical, and nanoscopic surface analyses using the modified mixing protocol that was confirmed in Phase I.

The dose-dependent effect of anti-adhesion was found in the screening process during the Exploratory Phase I in all groups. The lower doses (0.5 and 1.0 wt.%) maintained mechanical stability, but their anti-adhesion performance was lower; on the other hand, 1.5 and 2.0 wt.% delivered significantly better anti-adhesion performance without mechanical instability. Therefore, 0.5 and 1.0 wt.% were not selected, and only 1.5 and 2.0 wt.% progressed to Phase II.

2.2. Nanoparticle Synthesis, Phytochemical Profiling, and Crystallographic Characterization

The pumpkin fruit extract powder was purchased from Shaanxi Alibon Biotechnology Co., Ltd. (Xi'an, China; Batch No. RZL20250822-1). Based on the information from the Certificate of Analysis (CoA) provided by the manufacturer, the extract was obtained from the fruit portion via a hydro-alcoholic cold extraction method (70% ethanol/30% water at <40 °C) with a 10:1 extraction ratio. The moisture content (loss on drying) of the crude extract powder was 2.32% (USP<731>), while the particle size was 100% passage through 80 mesh (USP<786). The powder was then oven-dried (Model 202-00AB, China) at 30 °C to remove residual moisture. To complete a mechanical top-down size reduction, the dried material was milled in a planetary ball mill (Retsch GmbH, Haan, Germany) at 500 rpm for 10 h. To protect heat-sensitive organic compounds from thermal degradation, a daily 2 h intermittent milling cycle divided into 30 min runs with 15 min cooling intervals was applied to avoid heat buildup.

Particle Size Distribution: Particle size distribution, hydrodynamic diameter, and polydispersity index (PDI) for the fabricated plant extract powder were determined by Dynamic Light Scattering (DLS) using a 90Plus Particle Sizer instrument operating with 90Plus Particle Sizing Software Ver. 5.34 (Brookhaven Instruments Corp., Nashua, NH, USA). All measurements were carried out in deionized water at a temperature of 25.0 °C, a detection angle of 15.00°, a laser wavelength of 659.0 nm, a fluid refractive index of 1.330, and a viscosity of 0.890 cP. All the measurements were done in triplicate (10 s; overall 30 s). The plant extract showed an effective hydrodynamic diameter of 44.0 nm and a low PDI of 0.005. It is clearly stated here that DLS provides hydrodynamic diameter measurements of particles suspended in a liquid medium, not the dry primary particle size. Also, FE-SEM imaging was only used for the qualitative microstructural and morphological analysis of the particles embedded in the silicone medium. In contrast, quantitative parameters of particle size and distribution were determined by the DLS method only. Such characteristics indicate that the obtained extract nanoparticles comply fully with the requirements of nanoscale standardization ($\leq$100 nm hydrodynamic diameter and high particle size uniformity).

Then, the total contents of bioactive compounds in the pumpkin extract were quantitatively evaluated using established spectrophotometric assays. Total Phenolic Content (TPC) was determined via the Folin–Ciocalteu method and expressed as mg gallic acid equivalents (GAE)/100 g dry weight. Total Flavonoid Content (TFC) was quantified using the aluminum chloride colorimetric assay and expressed as mg rutin equivalents (RE)/100 g. Total alkaloids, glycosides, tannins, and carotenoids were determined spectrophotometrically according to standard procedures using atropine (at 470 nm), securidaside (Baljet's reagent at 495 nm), gelatin precipitation (at 540 nm), and acetone extraction protocols (measured at 480 and 510 nm), respectively. All spectrophotometric measurements were performed in triplicate.

Individual phenolic constituents were identified and quantified using a High-Performance Liquid Chromatography system coupled with a Diode Array Detector and Fraction Collector (HPLC-DAD, Sykam, Eresing, Germany). Chromatographic resolution was achieved on a Poroshell EC-C18 column (4.6 mm $\times$ 250 mm, 5 µm). The binary mobile phase architecture comprised distilled water with 0.1% glacial acetic acid (Solvent A) and acetonitrile with 0.1% glacial acetic acid (Solvent B), delivered at a constant flow rate of 1.0 mL/min. The linear gradient program was operated as follows: 0–3 min (60% A, 40% B), 8–10 min (20% A, 80% B), 10–15 min (10% A, 90% B), and 16–25 min (30% A, 70% B).

Samples were introduced at an injection volume of 100 µL while maintaining the column oven temperature at 30 °C. UV detection was recorded across a spectral range of 280–360 nm corresponding to the maximum absorption of the target compounds. Chromatographic analysis was performed to identify and quantify the major phenolic constituents present in the extract [12–18].

The crystalline structure and phase orientation of the synthesized sample were analyzed using an X-ray Diffractometer (PANalytical B.V., Almelo, The Netherlands). The instrument was operated with Cu $-$ Kα_1 radiation (λ = 1.54060 Å) generated at an accelerating voltage of 40 kV and a current of 8 mA, equipped with a nickel (Ni) Kβ filter (0.02 mm thickness). Diffractograms were acquired in continuous scanning mode over a 2θ angular range of 8.0054° to 99.9874° with a step size of 0.0110° and a step time of 6.12 s per step at 25.0 °C. The specimen was analyzed with sample stage rotation (spinning) to eliminate preferred orientation effects. Peak search and background determinations were performed using the default PANalytical software (Version 4.9, PANalytical B.V., Almelo, The Netherlands) suite with Profile/Rietveld fitting (Chi Square = 1.97, R_{wp} = 0.08216). The primary peak appeared at 2θ = 20.4282° (d = 4.34 Å) with a measured FWHM of 0.2110°. Crystallite size calculations via Scherrer analysis (K = 0.89) accounted for instrumental

broadening, and phase reflections were tentatively indexed against database patterns (JCPDS 96-715-4787 and JCPDS 96-220-2734).

2.3. Phase I Workflow: Optimization and Screening

To reduce the intense hydrodynamic resistance and viscosity of the siloxane bulk matrix, Phase I studied two different processing methods to achieve homogeneous nanofiller inclusion:

Method A (Base-Mediated Vacuum Mixing): The measured mass of PE-NPs was directly added into the VST-50 silicone elastomer (Factor II, Inc., Lakeside, AZ, USA; lot number B 092723-1LB; hardness Shore A 30) and mixed in a 10-to-1 ratio (base to catalyst) by weight. All samples were tested after curing at room temperature (23 ± 2 °C) for at least 16 h. The weight percentage (wt.%) of the incorporated plant extract powder was strictly defined relative to the total mass of the silicone polymer system (Base + Catalyst). To maintain precise base-to-catalyst stoichiometry, the weight of the added extract was subtracted from the base component, then the base–nanoparticle was processed in a vacuum mixer (SCALA Vacuum Mixer, Mestra, Bilbao, Spain) at 360 rpm for an initial cycle of 7 min. A 5 min stabilization pause followed this. Subsequently, the silicone catalyst component was introduced into the base–nanoparticle mixture at the manufacturer-specified 10:1 ratio, and the final composite was subjected to a second vacuum mixing cycle for 5 min to eliminate micro-air entrapment [19].

Method B (Catalyst-Mediated Stirring Integration): The same VST-50 silicone matrix, mixing ratio, curing protocol, and testing timeline described in Method A were utilized for Method B. The calculated mass of PE-NPs was first integrated directly into the low-viscosity silicone catalyst component. This mixture was magnetically stirred at a controlled speed at room temperature for 5 min, followed by a thermal stabilization pause to allow cooling. Afterwards, the combined catalyst–nanoparticle slurry was added to the silicone base elastomer (10:1 ratio), and the final composite was homogenized in the vacuum mixer for a single cycle of 5 min under negative pressure [20]. Field Emission Scanning Electron Microscopy (FE-SEM) (FEI Company, Eindhoven, The Netherlands) was immediately utilized to map and screen the microstructural dispersion efficiency of both techniques.

The process of thermal stabilization was adopted to ensure there would be no thermal build-up and mechanical degradation within the milling and mixing processes. The temperatures during all the processes had to be monitored to make sure that the temperature was well below 40° C.

During powder production, the ball milling process took up to 2 h in a day, with each process cycle lasting 30 min and cooling intervals of 15 min in between. During the addition of the silicone, the extract was mixed for 10 min using a magnetic stirrer without any heat, and after a 5 min stabilization interval, it was added to the silicone base. This was later mixed under vacuum for 5 min.

In addition to that, the curing characteristics of the silicone formulations were noted during the entire process of preparation. Because of adding the low-moisture (2.32%) extract powder, there was no inhibition observed in any way that could deviate from the normal curing schedule of the manufacturer (working time being 20–30 min and curing time being 6–8 h at room temperature, Factor II, Inc.). The functional maintenance of crosslinking density was confirmed by complete polymerization in solid state without the presence of any surface tackiness or phase separation.

For baseline screening, a matrix of 130 specimens was cast using custom-designed, CNC-machined translucent acrylic molds assembled with chloroform adhesive and G-clamps. All specimens were directly cast into their individual mold cavities at their exact intended dimensions without any post-casting cutting processes to avoid microdefects.

Specimens were assigned across five concentration groups (0, 0.5, 1.0, 1.5, and 2.0 wt.%). For anti-adhesion evaluation, 10 within-batch replicate specimens were prepared from the formulation batch per group (n = 10, total N = 50).

For mechanical evaluations (Tear Strength and Shore A Hardness), initial Phase I testing was conducted on 5 specimens per group (n = 5) as an exploratory screening step. Driven by the noticeable anti-adhesion activity and favorable mechanical response observed at higher nanoparticle loadings, testing was fully completed (n = 10) for the control (0 wt.%) and higher concentration groups (1.5 and 2.0 wt.%), while intermediate groups (0.5 and 1.0 wt.%) maintained n = 5. Consequently, Phase I inferential analyses are framed as exploratory screening evaluations rather than an a priori sample-size driven protocol. Thus, a total of 40 specimens (N = 40) were evaluated for Tear Strength and 40 specimens (N = 40) for Shore A Hardness [21].

1. Bacterial Anti-Adhesion Assay: Approval for ethical issues for the current in vitro study was obtained from the Research Ethics Committee of the College of Dentistry, University of Baghdad (Ref. No. 1192226). Five clinical isolates of *S. epidermidis* were acquired as pre-existing anonymized specimens, isolated previously from peri-prosthetic swabs and retrieved from the departmental repository. Bacterial strains were cultured on Blood Agar and Mannitol Salt Agar and incubated aerobically at 37 °C for 24–48 h. Species identification and profiling were performed using the automated VITEK 2 Compact system (bioMérieux, Marcy-l'Étoile, France) [21].

A total of 50 silicone samples were tested using the 5 different concentrations (n = 10 samples per group). Each sample was an experimental unit. Before testing, all specimens were cleaned with 70% ethanol (Iraq) to eliminate surface contamination and then allowed to air-dry for 5 min to ensure complete alcohol evaporation. Specimens were weighed before and after drying until a constant weight was obtained to confirm the absence of residual solvent [9,22].

Each specimen was immersed in a standardized *S. epidermidis* bacterial suspension (comprising equal proportions of the five clinical isolates) calibrated to a 0.5 McFarland standard ($\sim 1.5 \times 10^8$ CFU/mL). After 1 h of incubation, each specimen was transported into a sterile tube containing 1 mL of sterile distilled water and vortexed for 60 s to detach the adherent bacteria from the silicone [21].

Ten-fold serial dilutions were generated, and 0.1 mL aliquots from the 10^{-3} dilution were distributed onto Mannitol Salt Agar plates and incubated aerobically at 37 °C for 24–48 h. Colony-forming units (CFU/mL) were calculated using Equation (1) [23]:

The lower limit of detection (LOD) was set at 1×10^4 CFU/mL and scaled absolute values (CFU/mL) were used for statistical evaluation.

$$\text{CFU/mL} = \frac{\text{Colony count} \times 10^3}{0.1\ \text{mL}} = \text{Colony count} \times 10^4 \quad (1)$$

The Bacterial Anti-Adhesion Rate (%) was subsequently calculated using Equation (2) [24]:

$$\text{Anti-Adhesion Rate}(\%) = \frac{\text{CFU}_{\text{control}} - \text{CFU}_{\text{treated}}}{\text{CFU}_{\text{control}}} \times 100 \quad (2)$$

where CFU control is the mean bacterial count (CFU/mL) of the untreated control group, and CFU treated is the mean bacterial count (CFU/mL) of the treated group.

2. Tear Strength Evaluation: Tear strength evaluation was done according to ISO 34-1:2022 [25] using un-notched angular specimens (Type B) with an angle of 90° ± 0.5° and a standard thickness of 2.0 ± 0.2 mm. The thickness of the specimen was determined at three different locations at the apex with the help of a digital caliper

(±0.01 mm), and the mean thickness (d) was used in all calculations. The test was performed on a computerized Universal Testing Machine (Laryee Technology Co., Ltd., Beijing, China) with a 1 KN load cell at a rate of 500 mm/min. Those specimens in which tearing started from a position other than the apex were proactively excluded, and the test was repeated until 10 valid specimens were obtained for control and higher concentrations and 5 specimens for lower concentrations. Tear strength (Ts) in N/mm was calculated by the formula: Ts = F{max}/d, where F{max} is the maximum tear force (N), and d is the thickness (mm).

3. Shore A Hardness Assessment: Specimens (6 ± 0.05 mm thickness) were measured using a calibrated Zwick analog durometer (Shore A Durometer, ZwickRoell, Ulm, Germany) following ISO 48-4:2018 [26]. Five distinct measurements were taken per sample, with each point located at least 6 mm from the specimen edges and adjacent test points.

The chemical compatibility of each pilot group was evaluated via Fourier Transform Infrared Spectroscopy (FTIR; IRAffinity-1, Shimadzu, Japan) in Attenuated Total Reflectance (ATR) configuration. The spectra were recorded within the wavenumber range of 4000–400 cm^{-1}, at a resolution of 4 cm^{-1}, performing 21 scans for each spectrum using Happ-Genzel, followed by standard baseline correction and vector normalization.

2.4. Phase II Workflow: Advanced Definitive Testing

After the microstructural selection of Method B as the standard fabrication protocol during Phase I, Phase II advanced to a definitive sample design comprising 90 specimens, divided into three test blocks (n = 10 per group: Control (0 wt.%), 1.5 wt.%, and 2.0 wt.%). Specimens were post-cured at 23 ± 2 °C and conditioned at 50 ± 10% relative humidity for at least 16 h before physical evaluation in strict compliance with ISO 23529:2016 [27]. The definitive testing analyses involved:

1. Tensile and Elongation Testing: Tensile properties were obtained in accordance with ISO 37:2017 [28] for type 2 dumbbell specimens (75 mm overall, 20 mm gauge length, narrow width of 4 mm, thickness of 2.0 ± 0.2 mm). Pre-tensioning to 0.1 MPa was followed by tensile testing to failure at a constant crosshead speed of 500 mm/min. Ultimate tensile strength (UTS), in units of MPa, was calculated using the formula UTS = Fm/A_0, where Fm was the maximum force (N), and A_0 was the initial cross-sectional area of 8.00 mm^2. Any specimen that broke outside the 20 mm gauge length was excluded.
2. Macroscopic Surface Roughness (Ra): The roughness of the surface (Ra) was assessed according to ISO 21920-2:2021 [29] by employing a hand-held surface roughness measuring device (TR100, Dakota Ultrasonics, Scotts Valley, CA, USA). Measurement was done using a diamond probe with a cut-off wavelength (λc) of 0.8 mm and an overall trace length of 6 mm. The device was calibrated with a standardized reference block before the test. A total of three independent traces were measured in various locations on the smooth testing surface of each sample, and the average Ra (μm) was calculated for each sample (n = 10 per group).
3. Water Contact Angle Measurement: Water contact angle was determined using the sessile drop technique for the evaluation of wettability of surfaces using an optical tensiometer (Attension Theta, Biolin Scientific, Gothenburg, Sweden) controlled using OneAttension software Version 1.0. The tests were carried out at standard room temperature and humidity (23 ± 2 °C, 50 ± 5% RH). A volume of 2.96 μL of distilled water was dispensed on the center of the upper flat side of each sample by means of the automatic dispensing machine. A high-speed imaging technique was employed to acquire images of the drop. Contact angles (θ) were then measured as the average

of the left and right contact angles (CAleft and CARight) when the drop was in equilibrium (n = 10 per group).

2.5. Advanced Material Characterization

Surface Morphology and Elemental Composition (FE-SEM-EDX)

The surface morphology, microstructure, and elemental distribution of the prepared samples were evaluated using Field Emission Scanning Electron Microscopy (FE-SEM; Inspect f 50, FEI Company, Eindhoven, The Netherlands) equipped with an Energy-Dispersive X-ray Spectroscopy system (Axia ChemiSEM, Thermo Fisher Scientific, Waltham, MA, USA). To prevent electrostatic surface charging, samples were sputter-coated with a thin conductive gold layer (~1 nm). Micrographs and elemental mappings (C, O, and Si) were acquired using an Everhart-Thornley Detector (ETD) (Thermo Fisher Scientific, Waltham, MA, USA) at an accelerating voltage of 30.00 kV, a spot size of 3.5, and working distances (WDs) ranging between 5.0 mm and 18.9, with magnifications from 20,000× up to 140,000×. Elemental quantification was normalized to 100% on both wt% and at% bases across multiple representative surface regions to confirm topological homogeneity and structural reproducibility.

Atomic Force Microscopy and Surface Topography (AFM)

Parameters describing surface roughness, 3D surface topography, and quantitative distribution of nanoparticles in each experimental group, including pure (powder), silicone matrix, and nanocomposites with 1.5% and 2.0% nanoparticle concentrations, were studied by means of Atomic Force Microscopy (Flex-Axiom AFM, Nanosurf AG, Liestal, Switzerland). Raw topographical data were processed, form-leveled using a 3rd-order polynomial surface operator (LSP 3) and analyzed using MountainsSPIP® Academic software (v10.0.10510) according to the ISO 25178 [30] surface roughness standard. Main surface roughness parameters (root-mean-square height (Sq), arithmetic mean height (Sa), maximum height (Sz), skewness (Ssk), and kurtosis (Sku)) were measured within standardized 10 μm × 10 μm (10,000 nm × 10,000 nm) scan areas. Nanoparticle metrics, including mean nanoparticle diameter, total number, percentage of surface coverage, and density (number of nanoparticles in mm^2) were assessed using threshold-based detection algorithms within representative 4.04 μm × 4.04 μm to 4.17 μm × 4.17 μm surface areas. All topography measurements were performed in triplicate within separate sample areas across the evaluated sample groups.

To ensure intra-group constituent uniformity and maintain methodological consistency, each concentration group in Phase I and Phase II was prepared from a dedicated single batch of silicone, mixed and cured under standardized environmental conditions. Moreover, to avoid any operator bias during testing, specimen evaluation was randomized, and testing operators were blinded to the group concentration codes during mechanical and microbiological assays.

2.6. Statistical Analysis

Statistical analysis and data visualization were accomplished using OriginPro software (OriginPro 2026 Learning Edition, OriginLab Corporation, Northampton, MA, USA). Data normality and homogeneity of variance were evaluated using the Shapiro–Wilk and Levene's tests, respectively. For normally distributed datasets with homogeneous variances ($p > 0.05$), standard one-way Analysis of Variance (ANOVA) was performed, followed by Tukey's post hoc test for pairwise comparisons; this approach was applied to antimicrobial adhesion activity, tear strength, percentage of elongation, surface roughness (R_a), and wettability (contact angle) analyses. On the other hand, when the assumption of homogeneity of variance was violated ($p < 0.05$), as observed in the Shore A hardness data, Welch's ANOVA

with the Games–Howell post hoc comparison was used. For non-normally distributed datasets ($p < 0.05$), such as ultimate tensile strength (UTS), data were analyzed using the non-parametric Kruskal–Wallis test followed by Dunn's post hoc analysis. The standard for statistical significance for all evaluation assays was established at $p < 0.05$.

For all statistical tests, test specimens prepared from the dedicated single batch of each concentration group were treated as within-batch replicate test specimens for exploratory comparisons. The sample size (n) was determined depending on the stage of the test as follows: anti-adhesion evaluation: A sample size of $n = 10$ was used in all concentration groups (0, 0.5, 1.0, 1.5, and 2.0 wt.%) and resulted in $N = 50$ samples. Tear Strength and Shore A Hardness: A sample size of $n = 10$ was tested for the control (0 wt.%) and high-concentration groups (1.5 and 2.0 wt.%), while $n = 5$ were tested for low-concentration groups (0.5 and 1.0 wt.%), and provided $N = 40$ samples per test type. Tensile Strength (Elongation at Break), Surface Roughness, and Wettability: Testing was performed only for the control (0 wt.%) and high-concentration (1.5 and 2.0 wt.%) groups using $n = 10$ per group and provided $N = 30$ samples per test type.

Ultimate tensile strength (UTS) was the key outcome measure used to determine the mechanical strength of silicone. The other outcome measures for this experiment were: tear strength, % elongation, Shore A hardness, surface roughness (Ra), optical contact angle, and Bacterial Anti-Adhesion Evaluation rate.

3. Results

3.1. Phase I FE-SEM Microstructural Selection and Phytochemical Profile

Phytochemical quantification of the mechanically milled pumpkin extract powder revealed a high density of bioactive components, as summarized in Table 1.

Table 1. Phytochemical and chromatographic profile of processed PE-NPs.

Phytochemical	Content
Total phenolic content	190.8 mg GAE/100 g
Total flavonoid content	96.8 mg rutin/100 g
Total alkaloids	45.6 mg/100 g
Total glycosides	22.9 mg/100 g
Total tannins	18.7 mg/100 g
Total carotenoids	88.9 mg/100 g
Gallic acid	150.3 ppm
Quercetin	139.8 ppm
Apigenin	128.7 ppm
Caffeic acid	116.9 ppm
Ferulic acid	108.7 ppm
Kaempferol	93.6 ppm
Luteolin	80.6 ppm

Preliminary microstructural examination through FE-SEM during the qualitative process screening revealed noticeable differences in the microstructure due to the processing procedures. Micrographs taken from samples fabricated according to Method A (conventional direct mixing procedure) indicated nanoparticle aggregation. On the contrary, Method B (catalytic integration) indicated a qualitatively more even structure with few defects (Figure 2). The results indicate that prior dispersion within the low-viscosity catalyst enabled the circumvention of the hydrodynamic barriers of the siloxane matrix. Thus, Method B was chosen to be the standard manufacturing technique for all subsequent specimens in Phases I ($n = 130$) and II ($n = 90$).

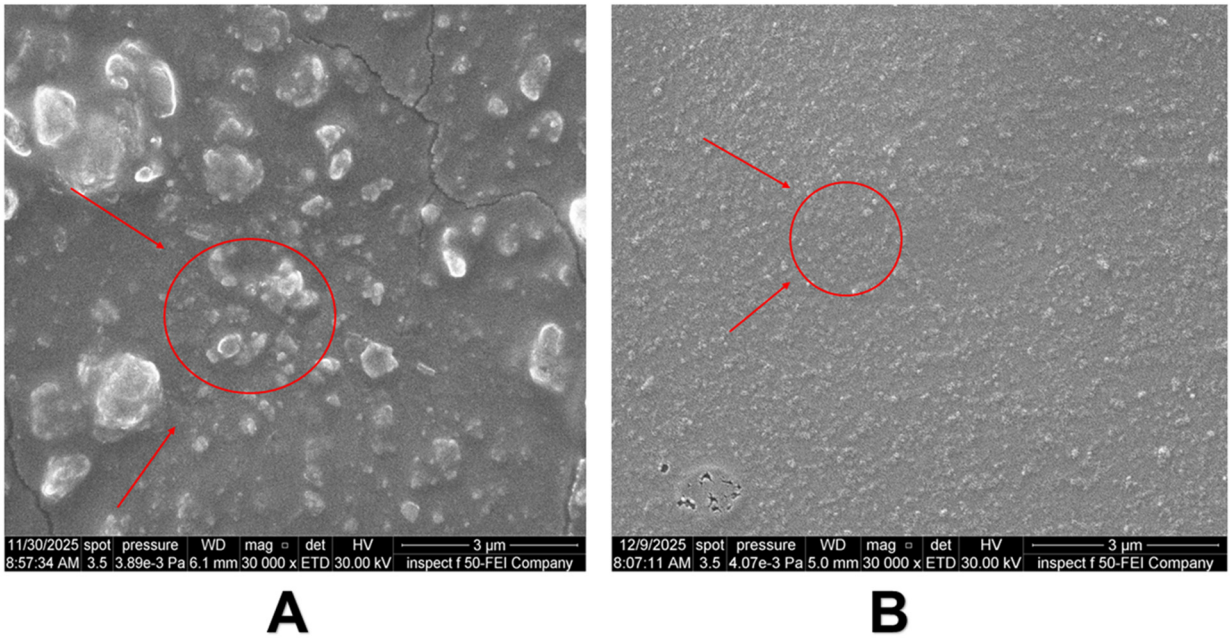


Figure 2. FE-SEM micrographs demonstrating the phase I screening of microstructural dispersion within the VST-50 matrix: (**A**) Method A (Conventional Direct Mixing) displaying prominent microstructural filler aggregation (red circle and arrows) under 30,000× magnification (scale bar = 3 µm), and (**B**) Method B (Catalyst-Mediated Integration) exhibiting highly homogeneous nanoparticle distribution (red circle and arrows) under 30,000× magnification (scale bar = 3 µm).

3.2. Phase I Screening: Material, Biological, and Baseline Mechanical Results

FTIR analysis shows that the distinctive peaks of the VST-50 matrix and PE-NPs persisted unchanged (Figure 3A), confirming physical entrapment without covalent modification. The XRD pattern of pure PE-NP powder displayed broad diffraction bands at (101), (110), and (200) planes (JCPDS Card No. 96-715-478) (Figure 3B). This amorphous/semi-crystalline profile confirms the organic nature of the nanoparticles, with the nanoscale size validated by the 44.0 nm DLS analysis.

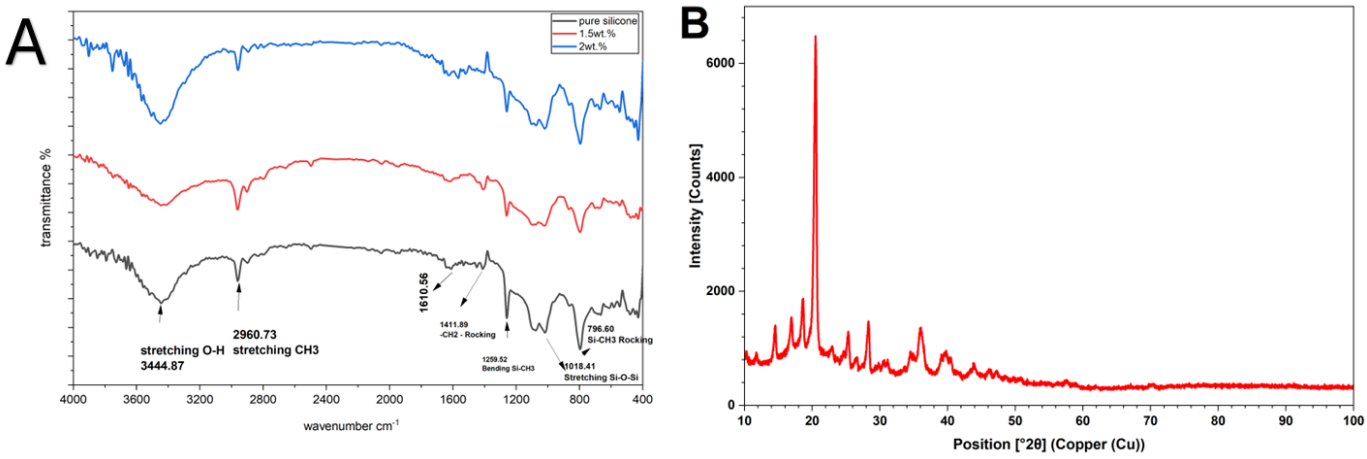


Figure 3. Spectroscopic and crystallographic characterization: (**A**) FTIR spectra of pure silicone, 1.5 wt.% and 2.0 wt.% PE-NP nanocomposites highlighting the primary physical entrapment bands (O-H stretching at 3444.87 cm^{-1} and Si-O-Si stretching at 1018.41 cm^{-1}), and (**B**) powder XRD pattern of the processed organic PE-NP powder verifying its amorphous/semi-crystalline phase distribution.

Biological screening against *S. epidermidis* revealed a significant, concentration-dependent anti-adhesion response ($p < 0.0001$), demonstrating a significant reduction

in bacterial colony-forming units (CFU) at higher nanofiller loading levels, with comprehensive descriptive and statistical variations listed in Table 2.

Table 2. Phase I screening outcomes: anti-adhesion activity, tear strength, and shore A hardness of the fabricated nanocomposites.

Statistical Test	Property	Control (Mean ± SD) (95% CI)	0.5 wt.% (Mean ± SD) (95% CI)	1.0 wt.% (Mean ± SD) (95% CI)	1.5 wt.% (Mean ± SD) (95% CI)	2.0 wt.% (Mean ± SD) (95% CI)	*p*-Value
One-way ANOVA	Anti-adhesion activity ($\times 10^4$ CFU/mL)	108.00 ^{a} ± 7.53 (102.61, 113.39)	59.70 ^{b} ± 6.80 (54.84, 64.56)	25.00 ^{c} ± 4.35 (21.89, 28.11)	18.80 ^{c} ± 6.03 (14.48, 23.12)	4.60 ^{d} ± 3.89 (1.82, 7.38)	<0.0001
One-way ANOVA	Tear strength (N/mm)	21.50 ^{d} ± 3.27 (19.16, 23.84)	34.80 ^{c} ± 3.63 (30.29, 39.31)	46.00 ^{b} ± 2.45 (42.96, 49.04)	52.63 ^{a} ± 6.58 (47.92, 57.34)	50.75 ^{a,b} ± 2.21 (49.17, 52.33)	<0.0001
Welch's ANOVA	Hardness (Shore A)	26.20 ^{c} ± 1.10 (25.41, 26.99)	29.84 ^{b} ± 0.11 (29.70, 29.98)	32.24 ^{a} ± 0.38 (31.76, 32.72)	30.64 ^{b} ± 0.83 (30.05, 31.23)	30.02 ^{b} ± 0.45 (29.70, 30.34)	<0.0001

Note: Values are expressed as Mean ± SD (95% Confidence Intervals in parentheses). Sample size: n = 10 within-batch replicate specimens for anti-adhesion activity (all groups) and for Tear/Hardness (0, 1.5, and 2.0 wt.% groups); n = 5 within-batch replicate specimens for Tear/Hardness (0.5 and 1.0 wt.% groups). Means within the same row sharing different superscript letters ($^{a-d}$) denote statistically significant differences ($p < 0.05$). Anti-adhesion values represent scaled CFU/mL considering the 10^{-3} dilution and 0.1 mL plated volume (10^4 scaling factor). Lower limit of detection (LOD) = 1.0 × 10^4 CFU/mL.

Standard mechanical assessment revealed that adding PE-NPs significantly changed both tear resistance and Shore A hardness ($p < 0.0001$). Tear strength demonstrated a consistent increase, reaching its peak at 1.5 wt.% loading. Hardness, on the other hand, increased gradually from the control before plateauing safely within clinical limits at higher concentrations, as listed systematically in Table 2 and Figure 4.

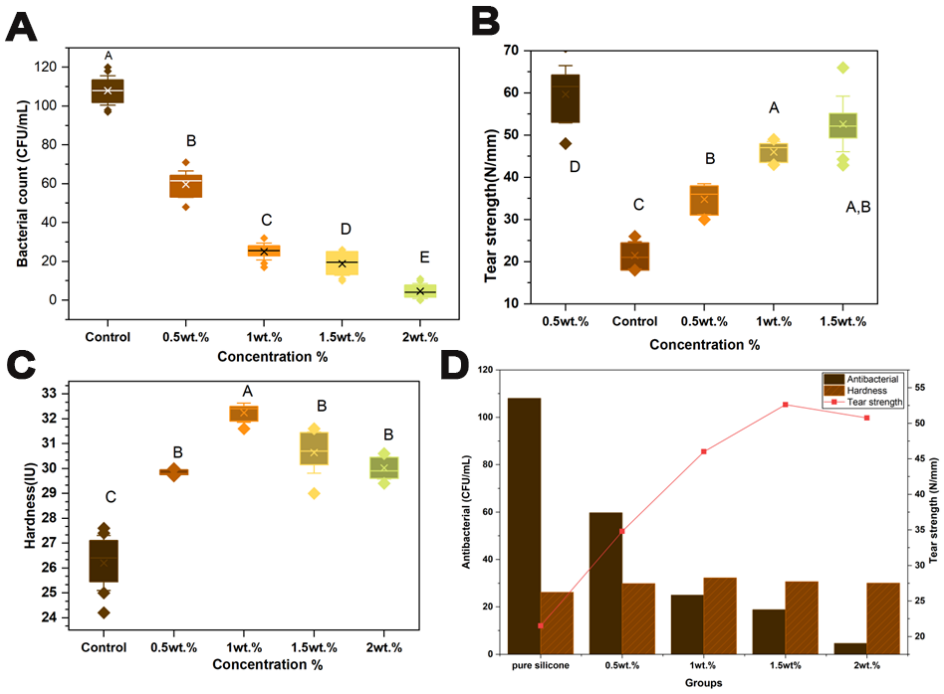


Figure 4. Phase I baseline biological and mechanical screening profiles across different PE-NP concentrations: (**A**) Anti-adhesion activity against *S. epidermidis* (CFU/mL), (**B**) tear strength (N/mm), (**C**) Shore A hardness, and (**D**) comparative interrelationship bar-line chart. Box plots designate the interquartile range (IQR), horizontal lines represent the median, and (×) denotes the mean. Groups with different superscript letters (A–E) are statistically significant at $p < 0.0001$.

3.3. Phase II Definitive Mechanical and Physical Results

Definitive mechanical testing showed that the organic nanoparticles significantly reinforced the siloxane matrix without causing brittleness. Ultimate tensile strength (UTS) and percentage of elongation mirrored each other's performance trends, with both increasing to highly significant optimal peaks at the 1.5 wt.% loading threshold before undergoing a sub-optimal decrease at the maximum 2.0 wt.% concentration.

Regarding macroscopic surface properties, statistical analysis displayed that variations in both profilometer-measured surface roughness (Ra) and optical contact angle wettability were not statistically significant, thereby maintaining the structural texture and important hydrophobic character of the silicone surface. All definitive physical and mechanical measures of the required concentrations are listed in Table 3 and Figure 5.

Table 3. Phase II definitive material characterization: ultimate tensile strength, elongation percentage, surface roughness (Ra), and contact angle wettability of the nanocomposites.

Statistical Test	Property	Control	1.5 wt.%	2.0 wt.%	*p*-Value
Kruskal–Wallis	Tensile strength (MPa) *	8 (8–9) ^{c}	10 (10–10.25) ^{a}	9.5 (8.75–10) ^{ab}	<0.0001
One-way ANOVA	Percent of Elongation (%)	494.14 ^{c} ± 27.59 (474.40, 513.88)	592.26 ^{a} ± 47.97 (557.94, 626.58)	545.18 ^{b} ± 41.84 (515.25, 575.11)	<0.0001
One-way ANOVA	Roughness (µm)	1.03 ± 0.21 (0.88, 1.18)	0.88 ± 0.13 (0.78, 0.97)	0.93 ± 0.21 (0.78, 1.08)	0.1831
One-way ANOVA	Wettability (°)	107.28 ± 8.23 (101.39, 113.17)	106.96 ± 8.14 (101.14, 112.79)	113.58 ± 3.22 (111.27, 115.88)	0.0731

Note: Data for Tensile Strength (*) are presented as Median (IQR) due to non-normal distribution. Data for Elongation, Roughness, and Wettability are presented as Mean ± SD (95% CI). Different superscript letters ($^{a–c}$) within the same row indicate statistically significant differences ($p < 0.05$).

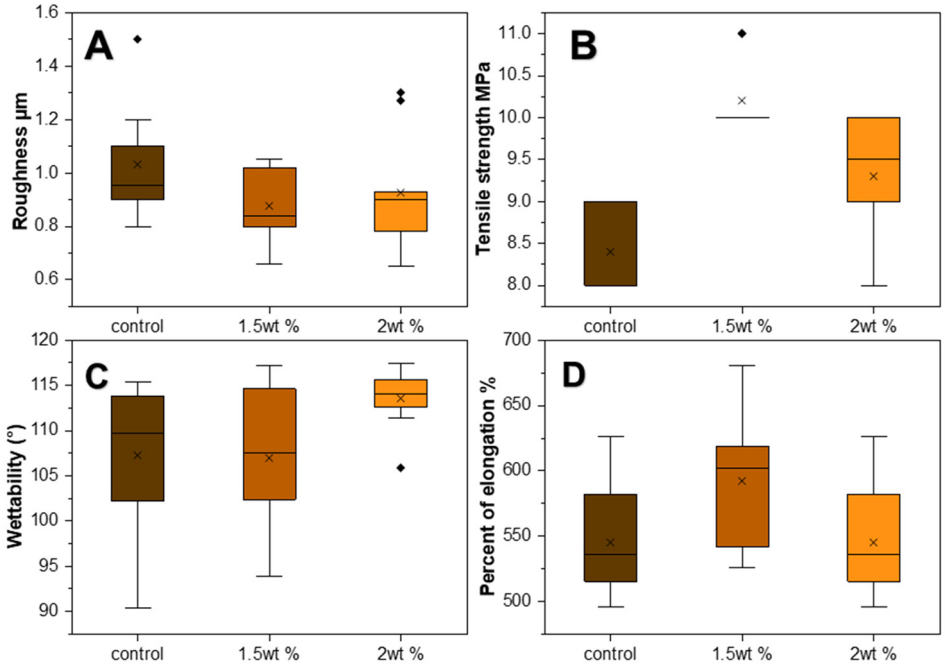
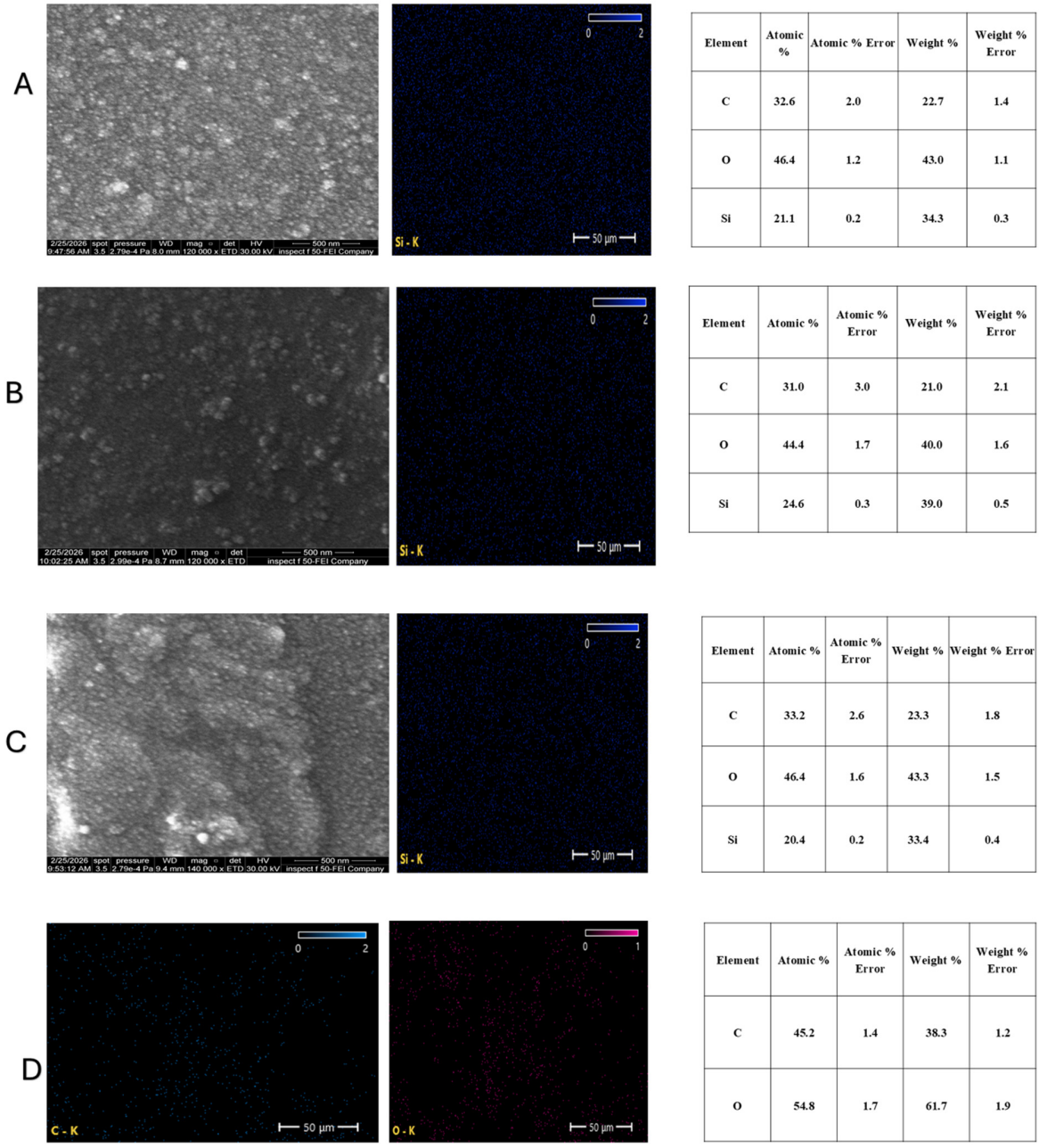


Figure 5. Phase II definitive physical and mechanical properties: (**A**) Macroscopic surface roughness (R_a, µm), (**B**) ultimate tensile strength (UTS, MPa), (**C**) optical contact angle wettability (°), and (**D**) elongation percentage (%). Box plots define the IQR, horizontal lines indicate the median, and (×) signifies the mean ($n = 10$ per group). Statistical thresholds are indicated via post hoc pairwise alignments, where $p < 0.0001$.

3.4. Advanced Structural and Topographical Nanometrology

Advanced FE-SEM imaging showed the PE-NPs as irregularly spherical structures ranging from 28 to 57 nm in diameter. Elemental composition mapped via EDX confirmed the organic nature of the nanofiller, tracking a clear composition of 38.3% carbon and 61.7% oxygen. In the polymer nanocomposites, EDX successfully confirmed uniform filler dispersion at 1.5 wt.% and documented systematic shifts in elemental distribution at 2.0 wt.% (with carbon increasing to 23.3% and oxygen to 43.3% relative to the control matrix baseline), confirming successful integration within the bulk crosslinked siloxane network as shown in Figure 6.



Element	Atomic %	Atomic % Error	Weight %	Weight % Error
C	32.6	2.0	22.7	1.4
O	46.4	1.2	43.0	1.1
Si	21.1	0.2	34.3	0.3

Element	Atomic %	Atomic % Error	Weight %	Weight % Error
C	31.0	3.0	21.0	2.1
O	44.4	1.7	40.0	1.6
Si	24.6	0.3	39.0	0.5

Element	Atomic %	Atomic % Error	Weight %	Weight % Error
C	33.2	2.6	23.3	1.8
O	46.4	1.6	43.3	1.5
Si	20.4	0.2	33.4	0.4

Element	Atomic %	Atomic % Error	Weight %	Weight % Error
C	45.2	1.4	38.3	1.2
O	54.8	1.7	61.7	1.9

Figure 6. Morphological and elemental nanometrology: (**A**–**C**) FE-SEM micrographs, corresponding Si elemental mappings, and quantitative EDX elemental tables for (**A**) pure silicone, (**B**) 1.5 wt.% nanocomposite, and (**C**) 2.0 wt.% nanocomposite (scale bars = 500 nm for micrographs, 50 µm for mapping blocks); (**D**) high-resolution EDX mapping and elemental composition table of the raw pure PE-NP powder tracking carbon (C-K) and oxygen (O-K) signatures.

High-resolution 3D AFM topographies provided a profound understanding of nanoscale surface modifications. Pure VST-50 silicone demonstrated a high baseline nanoscale arithmetic mean roughness (Sa) of 63.69 nm, driven by inherent micro-voids formed during curing. At the optimal 1.5 wt.% loading level, the roughness decreased to 18.88 nm. This dramatic smoothing effect may be attributed to the finely milled nanoparticles (average diameter of 44 nm) fitting within and filling the matrix's structural micro-voids. However, at 2.0 wt.% loading, the nanoscale roughness increased to 43.47 nm, providing direct morphological proof of minor nanoparticle aggregation along the polymer surface boundaries, as shown in Figure 7.

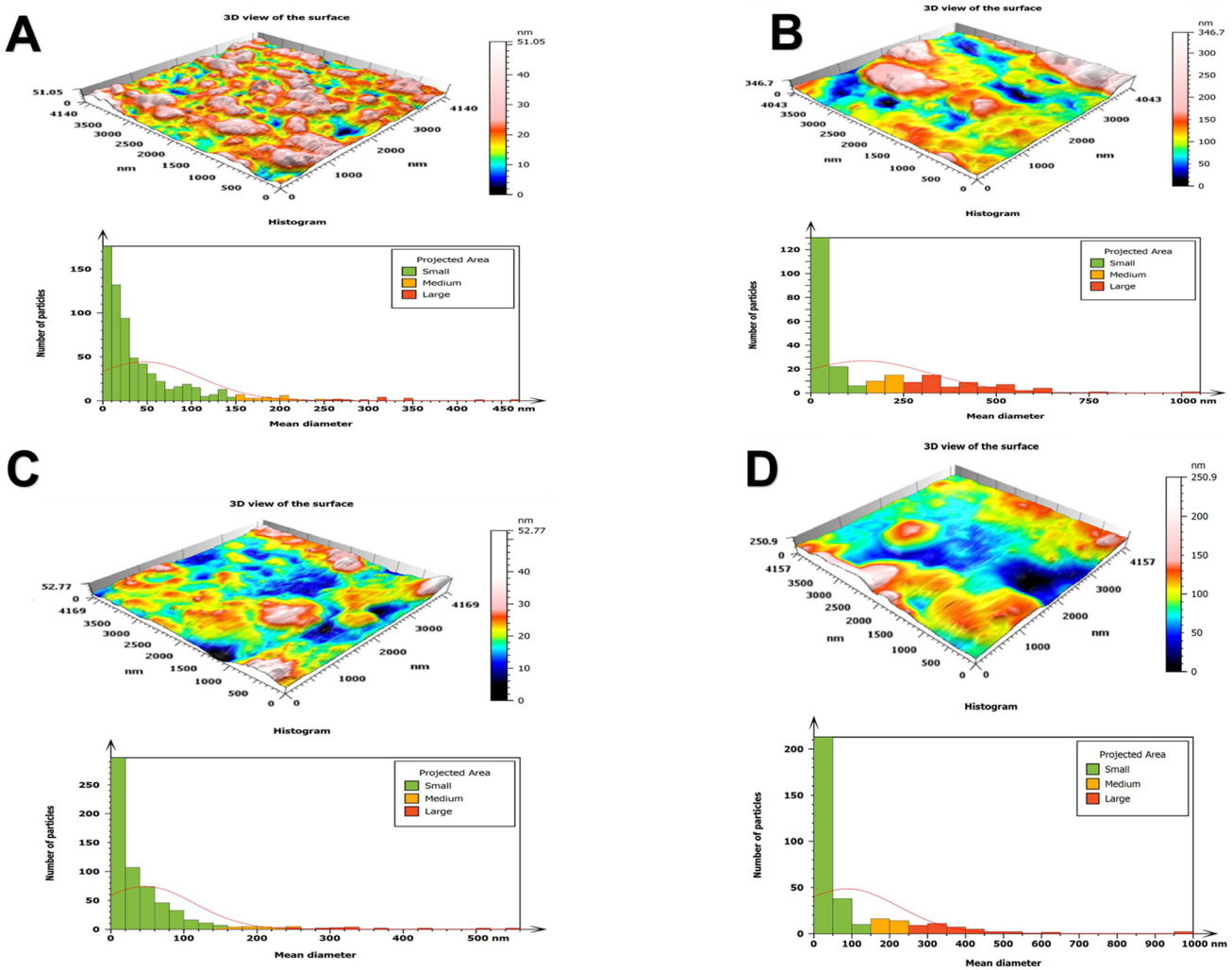


Figure 7. High-resolution 3D AFM topographical micrographs with synchronized particle size distribution histograms capturing nanostructure features and micro-void configurations for: (**A**) raw processed PE-NP powder, (**B**) pure unreinforced silicone matrix, (**C**) void-filled, structurally optimized 1.5 wt.% nanocomposite, and (**D**) 2.0 wt.% nanocomposite highlighting surface saturation and secondary particle re-agglomeration boundaries. Histograms were systematically generated using MountainsSPIP software via threshold detection, normalizing particle counts against mean diameters (nm) categorized by projected area fractions (nm^2) into small, medium, and large particle clusters.

4. Discussion

4.1. Nanoparticle Synthesis, Crystalline Structure, and Phytochemical Stability

The incorporation of pre-drying and high-energy ball milling (HEBM) has been shown to be essential for transforming bulk *Cucurbita pepo* extract into a highly reactive, nanoscale organic filler (44.0 nm via DLS). Despite HEBM using shear and impact forces that generate

localized thermal energy, the application of strict intermittent cooling cycles successfully protected the heat-sensitive phytochemicals. This preservation is quantitatively improved by the HPLC-DAD and spectrophotometric profiling, which isolated high concentrations of intact bioactive monomers (e.g., gallic acid, quercetin, and apigenin) [31–33].

XRD analysis was performed to analyze the physical state of the processed nanoparticles (PE-NPs). The characteristic diffraction peaks recorded at $2\theta \approx 14.47^{\circ}$,$18.57^{\circ}$, and 20.42° match the structure of cellulose type I crystalline material contained in plant-derived matrices. The broad amorphous halo underlying these peaks reflects the natural coexistence of amorphous biopolymers such as lignin, hemicellulose, and polyphenols. The pronounced broadening of these diffraction peaks after mechanical processing explains a significant reduction in crystallite size and increased structural disorder. Using the Scherrer equation, the average crystallite size was estimated at 17.26 nm. This structural refinement significantly increased the specific surface area, thereby increasing the accessibility of exposed bioactive functional groups for subsequent chemical and biological interactions within the polymer matrix [34–36].

4.2. Influence of Processing and Catalyst-Mediated Dispersion

High-viscosity siloxane bases can make it difficult to add organic fillers directly because of strong hydrodynamic barriers that cause particles to aggregate. Pre-dispersing the 44.0 nm PE-NPs into the low-viscosity silicone catalyst (Method B) produces a significant processing effect. Because the curing agent shows a significantly lower viscosity than the thick VST-50 base, mechanical stirring easily breaks the cohesive van der Waals forces that drive nanoparticle agglomeration in the dry state.

The subsequent vacuum mixing under negative pressure removed micro-air entrapment, producing a homogeneous composite. The result of this processing was visually confirmed by Phase I FE-SEM microstructural screening, where Method B successfully bypassed the matrix's hydrodynamic barriers to achieve uniform dispersion compared to the agglomerated networks seen in Method A [7,37].

4.3. Interfacial Bonding and Intermolecular Interactions

The FTIR spectra indicated that the addition of PE-NPs did not alter the primary covalent backbone of the VST-50 matrix, due to all experimental groups retaining the normal siloxane absorption bands (Si–O–Si stretching, Si–CH_3 bending, and CH_3 stretching). Instead, the minor shifts observed within the O–H and C = O regions show that secondary intermolecular physical interactions drive the reinforcement mechanism.

Organic PE-NPs contain an abundance of polyphenols and semicrystalline cellulose; this provides a high density of surface hydroxyl (OH) groups. These functional groups form extensive hydrogen bonding and stable dipole–dipole interactions with the electronegative oxygen atoms in the siloxane backbone of the polymer chain. These non-covalent yet dense interfacial cross-linking networks prevent the local segmental mobility of the polydimethylsiloxane (PDMS) chains against the nanoparticle surfaces. This interfacial adhesion may be attributed to efficient mechanical stress transfer across the polymer–filler boundaries [10,11].

4.4. Synergistic Anti-Adhesion Mechanisms

Concentration-dependent anti-adhesion activity against *S. epidermidis* may be due to the uniform nano-dispersion of the biogenic filler. *S. epidermidis* is an opportunistic pathogen whose primary virulence depends on cell surface hydrophobicity and biofilm formation on biomaterials. HPLC-DAD evaluation identified gallic acid (150.3 ppm) and quercetin (139.8 ppm) as the primary pharmacologically active constituents, assisted by flavones (apigenin, luteolin) and hydroxycinnamic acids (caffeic and ferulic acids).

Noticeable anti-adhesion activity may come from several different combined ways. Gallic acid directly alters bacterial membrane structure and disrupts cell metabolism, inhibiting biofilm formation. Quercetin downregulates the *ica* locus and reduces polysaccharide intercellular adhesin (PIA) production, thereby decreasing bacterial surface hydrophobicity and preventing initial pathogen attachment. Luteolin and ferulic acid rapidly disrupt cell membrane integrity, inducing leakage of intracellular contents and causing oxidative damage via exogenous reactive oxygen species (ROS). The background matrix of tannins and alkaloids acts synergistically by binding to key bacterial proteases, while carotenoids increase cell membrane permeability under osmotic stress. This multi-target biogenic barrier effectively results in 95.7% anti-adhesion activity rate at higher loadings without relying on synthetic agents that may present potential cytotoxicity [38–40].

4.5. Interrelationship Between Nano Topography, Surface Hygiene, and Mechanical Performance

4.5.1. Surface Roughness and Wettability

Nanoscale surface topography (AFM), macro-roughness (R_a), and biological resistance were all found to be significantly related. Unreinforced VST-50 silicone exhibits a high inherent nanoscale roughness (S_a = 63.69 nm), hypothesized to be influenced by micro-voids and granular porosities formed during curing. These micro-voids traditionally may act as protective structural niches that anchor bacteria and promote plaque accumulation.

The finely milled PE-NPs effectively fit within and fill these matrix micro-voids at 1.5 wt.% loading, reducing the nanoscale arithmetic mean roughness down to 18.88 nm. This significant smoothing effect reduces the physical spaces required for initial bacterial incubation.

While nano-topography was improved, macroscopic stylus roughness (R_a) and optical contact angles (>100°) remained statistically unchanged ($p > 0.05$). Maintaining the standard clinical macro-texture and hydrophobic character presents a desirable property in vitro, ensuring that the modified silicone maintains its natural resistance to fluid-mediated plaque attachment among the concentrations evaluated in this study [41,42].

4.5.2. Tear Strength, Tensile Properties, and Hardness

The mechanical performance measurements directly mirror the spatial distribution state of the nanofiller. Incorporating 1.5 wt.% PE-NPs induced a highly significant 145% increase in tear strength (rising from 21.5 N/mm to 52.62 N/mm), alongside peak values for ultimate tensile strength 10 (10–10.25) MPa and elongation at break (592.26%). This outstanding reinforcement is governed by both chemical bonding and a physical energy dissipation mechanism [43].

Physically, when the material is exposed to external tearing or stretching forces, the well-dispersed, high-surface-area nanoparticles may act as rigid interlocking nodes that bridge propagating cracks. When an advancing crack front meets these uniformly distributed PE-NPs, it is either arrested or forced to branch out into multiple micro-cracks (crack branching theory). This configuration scatters and dissipates mechanical strain energy near the apex of the flaws, requiring a significantly higher ultimate load to cause structural failure. This parameter is potentially advantageous for mitigating marginal degradation of thin prosthetic borders (e.g., nasal or auricular margins) during routine patient removal and cleaning cycles [5].

Shore A hardness slowly increased from 26.2 Shore A units (control) before plateauing safely at 30.6 Shore A units at 1.5 wt.%. This controlled increase confirmed that the filler prevents surface indentation and increases elastomeric stiffness without inducing brittleness, maintaining the prosthesis's hardness within the ideal clinical range (10–45 Shore A units) required to mimic natural facial soft tissues [44].

4.6. Evaluation of Agglomeration Behavior and Filler Limits

The sub-optimal decrease in tensile strength 9.5 (8.75–10) MPa, tear resistance (50.75 N/mm), and the significant increase in nanoscale AFM roughness (S_a = 43.47 nm) that are recorded at 2.0 wt.% indicate the optimal filler saturation limit among the concentrations evaluated in this study. When the nanoparticle concentration is higher than the physical capacity of the siloxane matrix, the inter-particle distance reduces below a critical limit. At this stage, the high surface free energy of the organic nanoparticles causes cohesive van der Waals forces to control the mechanical shear forces generated during mixing.

Therefore, the nanoparticles aggregate again into small groups along the polymer boundaries. Instead of acting as reinforcing anchoring nodes, these dense clusters create structural discontinuities and micro-voids within the cross-linked network. Under external mechanical stress, these agglomerates easily detach or fracture, acting as localized stress concentration areas that accelerate crack initiation and affect material flexibility [5].

5. Conclusions

This study shows that mechanically milled Pumpkin Extract Nanoparticles act as a reinforcing and anti-adhesion agent for VST-50 maxillofacial silicone. Incorporating the nanoparticles via a multi-step catalyst-mediated stirring technique effectively facilitated processing within the siloxane matrix to promote homogeneous spatial dispersion.

The specific intermediate concentration among the concentrations evaluated in this study was identified as the optimal formulation in vitro, resulting in a statistically significant enhancement and a significant increase in ultimate tensile strength and elongation, while keeping Shore A hardness strictly within standard reference limits for maxillofacial elastomers. At the same time, the uniform exposure of bioactive phenolic compounds demonstrated initial in vitro anti-adhesion activity against *S. epidermidis* by smoothing nanoscale surface micro-voids without altering the material's baseline macro-roughness or essential hydrophobic integrity.

These results show promise for in vitro research to improve the qualities of maxillofacial prostheses in the context of this experiment design; however, further research is needed regarding long-term aging and biocompatibility studies.

6. Limitations and Future Recommendations

Although this investigation shows a promising natural reinforcement approach, certain limitations must be known before clinical transformation.

Long-term Leaching Kinetics: The desorption and release profiles of the encapsulated phytochemicals under simulated environmental and physiological fluids such as artificial sweat, sebum, or synthetic tears, and under artificial weathering conditions (UV radiation and thermal aging), require long-term estimation to assess long-term antimicrobial activity.

In Vitro Biocompatibility: Although the organic source of the filler supports its potential suitability, definitive cytocompatibility assays such as MTT colorimetric evaluations on human dermal fibroblasts are required to support the absence of localized cytotoxicity on the skin barrier.

Aesthetic Evaluation: Future research should evaluate the effect of PE-NP incorporation on the standard optical translucency, color stability, and color ability of the silicone matrix when mixed with standard intrinsic and extrinsic prosthodontic pigments to ensure ideal skin match.

Batch-to-Batch Variability: Because silicone test specimens for each evaluated concentration within Phase I and Phase II were derived from dedicated single preparation batches to guarantee intra-group constituent uniformity, potential batch-to-batch variations across

repeated mixing cycles were not assessed, representing a methodological limitation of the present study design.

Author Contributions: Conceptualization, T.M.A. and T.I.H.; methodology, T.M.A. and T.I.H.; software, T.M.A.; validation, T.I.H.; formal analysis, T.M.A. and T.I.H.; investigation, T.M.A.; resources, T.M.A. and T.I.H.; data curation, T.M.A.; writing—original draft preparation, T.M.A.; writing—review and editing, T.I.H.; visualization, T.M.A.; supervision, T.I.H.; project administration, T.M.A.; funding acquisition, T.M.A. and T.I.H. All authors have read and agreed to the published version of the manuscript.

Funding: This research received no external funding.

Institutional Review Board Statement: The study protocol for this in vitro investigation was approved by the Research Ethics Committee of the College of Dentistry, University of Baghdad, Iraq (Project No. 1192226, approval date: 7 April 2026).

Informed Consent Statement: Patient informed consent was waived as the clinical isolates were obtained as historical, fully de-identified diagnostic specimens retrieved from the departmental repository. The study involved strictly secondary in vitro laboratory evaluations on archived microbial strains without direct human subject contact or access to personal identifying information, in accordance with institutional ethical standards.

Data Availability Statement: The original contributions presented in this study are included in the article. Further inquiries can be directed to the corresponding authors.

Acknowledgments: The authors are appreciative of the Department of Prosthodontics, College of Dentistry, University of Baghdad, for their support in completing this research.

Conflicts of Interest: The authors declare no conflicts of interest.

References

1. Ghazali, N.; Romli, A.Z.; Tengku, M.A.; Tengku, F. Application of Silicone Elastomers in Extraoral Prosthesis: A Narrative Review. *Compend. Oral Sci.* **2025**, *12*, 20–39. [CrossRef]
2. Gradinariu, A.I.; Racles, C.; Stoica, I.; Stelea, C.G.; Simionescu, A.M.A.; Jehac, A.E.; Costan, V.V. Silicones for Maxillofacial Prostheses and Their Modifications in Service. *Materials* **2024**, *17*, 3297. [CrossRef] [PubMed]
3. Gradinariu, A.I.; Stoica, A.C.; Bargan, A.; Racles, C.; Stelea, C.G.; Costan, V.V. Color Modifications of a Maxillofacial Silicone Elastomer under the Effect of Cigarette Smoke. *Materials* **2024**, *17*, 4089. [CrossRef] [PubMed]
4. Otto, M. Staphylococcus Colonization of the Skin and Antimicrobial Peptides. *Expert Rev. Dermatol.* **2010**, *5*, 183–195. [CrossRef] [PubMed]
5. Kumail, A.F.; Hamad, T.I. Evaluation of Some Mechanical Properties of Room Temperature Maxillofacial Silicone after the Addition of Nano Barium Titanate. *Bionatura* **2023**, *8*, 1.
6. AbdulKareem, A.A.; Hamad, T.I. The Effects of Nano Alumina On Mechanical Properties of Room Temperature Vulcanized Maxillofacial Silicone (Pilot Study). *J. Bagh. Coll. Dent.* **2019**, *31*, 2722. [CrossRef]
7. Ali, A.A.; Safi, I.N. Impact of Nano-Cellulose Fiber Addition on Physico-Mechanical of Room Temperature Vulcanized Maxillofacial Silicone. *J. Taibah Univ. Med. Sci.* **2023**, *18*, 1616–1626. [CrossRef] [PubMed]
8. Salih, S.I.; Oleiwi, J.K.; Ali, H.M. Modification of Silicone Rubber by Added PMMA and Natural Nanoparticle Used for Maxillofacial Applications. *ARPN J. Eng. Appl. Sci.* **2019**, *14*, 781–791.
9. Sarraj, S.; Szymiczek, M.; Jurczyk, S. Influence of Herbal Fillers Addition on Selected Properties of Silicone Subjected to Accelerated Aging. *Polymers* **2022**, *15*, 42. [CrossRef] [PubMed]
10. Gavril, R.N.; Stoica, F.; Lipsa, F.D.; Constantin, O.E.; Stanciuc, N.; Aprodu, I.; Rapeanu, G. Pumpkin and Pumpkin By-Products: A Comprehensive Overview of Phytochemicals, Extraction, Health Benefits, and Food Applications. *Foods* **2024**, *13*, 2694. [CrossRef] [PubMed]
11. Shakir, D.A.; Abdul-Ameer, F.M. Effect of Nano-Titanium Oxide Addition on Some Mechanical Properties of Silicone Elastomers for Maxillofacial Prostheses. *J. Taibah Univ. Med. Sci.* **2018**, *13*, 281–290. [CrossRef] [PubMed]
12. Laouini, S.E.; Ouahrani, M.R. Phytochemical Screening, in Vitro and Antibacterial Activity of *Rumex vesicarius* L. Extract. *Sci. Study Res. Chem. Chem. Eng. Biotechnol. Food Ind.* **2017**, *18*, 367–376.

13. Habibatni, S.; Zohra, A.F.; Khalida, H.; Anwar, S.; Mansi, I.; Ali, N.A. In-Vitro Antioxidant, Xanthine Oxidase-Inhibitory and In-Vivo Anti-Inflammatory, Analgesic, Antipyretic Activity of *Onopordum acanthium*. *Int. J. Phytomed.* **2017**, *9*, 92–100. [CrossRef]
14. Ajanal, M.; Gundkalle, M.B.; Nayak, S.U. Estimation of Total Alkaloid in Chitrakadivati by UV-Spectrophotometer. *Anc. Sci. Life* **2012**, *31*, 198–201. [CrossRef] [PubMed]
15. Tofighi, Z.; Saeidi, N.G.; Hadjiakhoondi, A.; Yassa, N. Determination of Cardiac Glycosides and Total Phenols in Different Generations of *Securigera securidaca* Suspension Culture. *Res. J. Pharmacogn.* **2016**, *3*, 25–31.
16. Abdelkader, M.; Ahcen, B.; Rachid, D.; Hakim, H. Phytochemical Study and Biological Activity of Sage (*Salvia officinalis* L.). *Int. Sch. Sci. Res. Innov.* **2014**, *8*, 1253–1257.
17. Kumar, H.; Sharma, S. Determination of Chlorophyll and Carotenoid Loss in *Dalbergia sissoo* Caused by *Aonidiella orientalis* (Newstead) [Homoptera: Coccoidea: Diaspididae]. *J. Entomol. Zool. Stud.* **2014**, *2*, 104–106.
18. Krstonosic, M.A.; Hogervorst, J.C.; Mikulic, M.; Gojkovic-Bukarica, L. Development of HPLC Method for Determination of Phenolic Compounds on a Core Shell Column by Direct Injection of Wine Samples. *Acta Chromatogr.* **2019**, *32*, 134–138. [CrossRef]
19. Alanssari, B.F.; Khalaf, B.S. Effect of Addition of Composite Polyamide Micro Particles and Silicone Dioxide Nanoparticle on Some Mechanical Properties of Room Temperature Vulcanized Maxillofacial Silicone. *Indian J. Forensic Med. Toxicol.* **2020**, *14*, 1013–1019. [CrossRef]
20. Wang, L.; Liu, Q.; Jing, D.; Zhou, S. Biomechanical Properties of Nano-TiO_2 Addition to a Medical Silicone Elastomer: The Effect of Artificial Ageing. *J. Dent.* **2014**, *42*, 475–483. [CrossRef] [PubMed]
21. Kareem, Y.M.; Hamad, T.I. Assessment of the Antibacterial Effect of Barium Titanate Nanoparticles against *Staphylococcus epidermidis* Adhesion after Addition to Maxillofacial Silicone. *F1000Research* **2023**, *12*, 385. [CrossRef]
22. Darwai, A.; Jain, N. Development of Method for Extraction and Validation Crude Drugs from Plant Extract. *Asian J. Pharm. Educ. Res.* **2022**, *11*, 47–67.
23. Taha, N.R.; Abass, S.M. *Cordia myxa* Fruit Extract Antibacterial Efficacy and Its Effect on the Surface Roughness of Heat-Cured Acrylic Denture Base Material. *Prosthesis* **2025**, *7*, 48. [CrossRef]
24. Wang, N.; Ji, Y.; Zhu, Y.; Wu, X.; Mei, L.; Zhang, H.; Deng, J.; Wang, S. Antibacterial Effect of Chitosan and Its Derivative on *Enterococcus faecalis* Associated with Endodontic Infection. *Exp. Ther. Med.* **2020**, *19*, 3805–3813. [CrossRef] [PubMed]
25. *ISO 34-1:2022*; Rubber, Vulcanized or Thermoplastic—Determination of Tear Strength—Part 1: Trouser, Angle and Crescent Test Pieces. International Organization for Standardization: Geneva, Switzerland, 2022.
26. *ISO 48-4:2018*; Rubber, Vulcanized or Thermoplastic—Determination of Hardness—Part 4: Indentation Hardness by Durometer (Shore Hardness). International Organization for Standardization: Geneva, Switzerland, 2018.
27. *ISO 23529:2016*; Rubber—General Procedures for Preparing and Conditioning Test Pieces for Physical Test Methods. International Organization for Standardization: Geneva, Switzerland, 2016.
28. *ISO 37:2017*; Rubber, Vulcanized or Thermoplastic—Determination of Tensile Stress-Strain Properties. International Organization for Standardization: Geneva, Switzerland, 2017.
29. *ISO 21920-2:2021*; Geometrical Product Specifications (GPS)—Surface Texture: Profile—Part 2: Terms, Definitions and Surface Texture Parameters. International Organization for Standardization: Geneva, Switzerland, 2021.
30. *ISO 25178-2:2021*; Geometrical Product Specifications (GPS) — Surface Texture: Areal — Part 2: Terms, Definitions and Surface Texture Parameters. International Organization for Standardization: Geneva, Switzerland, 2021.
31. Bekele, D.W.; Emire, S.A. Effects of Pre-Drying Treatment and Particle Sizes on Physicochemical and Structural Properties of Pumpkin Flour. *Heliyon* **2023**, *9*, e21609. [CrossRef] [PubMed]
32. Borhan, M.Z.; Ahmad, R.; Rusop, M.; Abdullah, S. Optimization of Ball Milling Parameters to Produce *Centella asiatica* Herbal Nanopowders. *J. Nanostructure Chem.* **2013**, *3*, 79. [CrossRef]
33. Ciarlantini, C.; Piozzi, A.; Ammendola, S. The Planetary Ball Milling of Different Powders Yields Similar Granulometry. *Nano Med. Mater.* **2025**, *5*, 2466. [CrossRef]
34. Chibac-Scutaru, A.L.; Podasca, V.; Dascalu, I.A.; Melinte, V. Exploring the Influence of Synthesis Parameters on the Optical Properties for Various CeO2 NPs. *Nanomaterials* **2022**, *12*, 1402. [CrossRef] [PubMed]
35. Rabiei, M.; Palevicius, A.; Monshi, A.; Nasiri, S.; Vilkauskas, A.; Janusas, G. Comparing Methods for Calculating Nano Crystal Size of Natural Hydroxyapatite Using X-Ray Diffraction. *Nanomaterials* **2020**, *10*, 1627. [CrossRef] [PubMed]
36. Alsaiari, N.S.; Alzahrani, F.M.; Amari, A.; Osman, H.; Harharah, H.N.; Elboughdiri, N.; Tahoon, M.A. Plant and Microbial Approaches as Green Methods for the Synthesis of Nanomaterials: Synthesis, Applications, and Future Perspectives. *Molecules* **2023**, *28*, 463. [CrossRef] [PubMed]
37. Radey, N.S.; Al Shimy, A.M.; Ahmed, D.M. Effect of Extraoral Aging on Mechanical Properties of Facial Silicone Elastomer Reinforced With Titanium-Oxide Nanoparticles (In Vitro Study). *Alex. Dent. J.* **2020**, *45*, 29–36. [CrossRef]
38. Zhang, Z.; Cao, M.; Shang, Z.; Xu, J.; Chen, X.; Zhu, Z.; Wang, W.; Wei, X.; Zhou, X.; Bai, Y.; et al. Research Progress on the Antibacterial Activity of Natural Flavonoids. *Antibiotics* **2025**, *14*, 334. [CrossRef] [PubMed]

39. Tyagi, B.; Dubey, A.; Verma, A.K.; Tiwari, S. Antibacterial Activity of Phenolics Compounds against Pathogenic Bacteria. *Int. J. Pharm. Sci. Rev. Res.* **2015**, *35*, 16–18.
40. Walsh, D.J.; Livinghouse, T.; Goeres, D.M.; Mettler, M.K.; Stewart, P.S. Antimicrobial Activity of Naturally Occurring Phenols and Derivatives Against Biofilm and Planktonic Bacteria. *Front. Chem.* **2019**, *7*, 653. [CrossRef] [PubMed]
41. Ali, M.S.; Abdul-Ameer, F.M. Evaluating the Mechanical Properties of Maxillofacial Silicone Enhanced by Hexagonal Boron Nitride Particles. *Baghdad Sci. J.* **2025**, *22*, 3017–3025. [CrossRef]
42. Sonnahalli, N.K.; Chowdhary, R. Effect of Nanoparticles on Color Stability and Mechanical and Biological Properties of Maxillofacial Silicone Elastomer: A Systematic Review. *J. Indian Prosthodont. Soc.* **2020**, *20*, 244–254. [CrossRef] [PubMed]
43. Ganesan, K.; Kornhuber, S.; Dhivakar, M.J.; Sarathi, R.; Danikas, M.G. Investigation on the Role of Interface on Electrical, Thermal and Mechanical Properties of Silicone Rubber-BN Nanocomposites. *J. Eng. Sci. Technol. Rev.* **2024**, *17*, 16–22. [CrossRef]
44. Kumail, A.F.; Hamad, T.I. Impact of Shore A Hardness and Surface Roughness of Room Temperature Maxillofacial Silicone after the Addition of Nano Barium Titanate. *Bionatura* **2023**, *8*, 1. Available online: https://www.revistabionatura.com/files/2023.08.03.88.pdf (accessed on 1 July 2026).

Disclaimer/Publisher's Note: The statements, opinions and data contained in all publications are solely those of the individual author(s) and contributor(s) and not of MDPI and/or the editor(s). MDPI and/or the editor(s) disclaim responsibility for any injury to people or property resulting from any ideas, methods, instructions or products referred to in the content.